CrossMark

ORIGINAL ARTICLE

A methodology for quantifying the impact of casting procedure on anisotropy in fiber-reinforced concrete using X-ray CT

Tyler Oesch (ID) · **Eric Landis** · **Daniel Kuchma**

Abstract Fiber-reinforced concretes (FRCs) offer significant improvements in tensile strength and durability compared to most other concrete mixes. However, for safe and efficient use of FRC in large structures, anisotropy of fiber orientation needs to be understood and properly controlled. In this project, both cored samples extracted from a FRC slab and FRC samples cast individually in molds were assessed using X-ray computed tomography (CT) and measurements of fiber orientation were extracted from the resulting CT images. These results showed that fibers within the slab were highly anisotropic in orientation while fibers in individually cast samples showed a much more heterogeneous distribution of orientations. This indicates that fiber orientation is highly dependent on the casting process and suggests that FRC can only be safely and efficiently utilized if anisotropic fiber orientation is properly accounted for during design and optimized casting methods are used during construction.

The original version of this article was revised due to a retrospective Open Access order.

T. Oesch (✉)
Bundesanstalt für Materialforschung und -prüfung (Federal Institute for Materials Research and Testing), Berlin, Germany
e-mail: tyler.oesch@bam.de

E. Landis
Department of Civil and Environmental Engineering, University of Maine, Orono, ME, USA

D. Kuchma
Department of Civil and Environmental Engineering, Tufts University, Medford, MA, USA

1 Introduction

1.1 Structural use of FRC

Significant elongation is needed for steel reinforcing bars to carry substantial tensile loads within concrete components. This elongation results in the formation of cracks in the surrounding concrete material and, if these cracks are wide, they can be unsightly and can lead to durability problems through the movement of chlorides causing corrosion to the steel reinforcing bars. The size and spacing of reinforcing steel is a dominant factor in determining the size of cracks [1].

FRC may be viewed as reinforced concrete with extremely small and closely-spaced reinforcing bars. Its use in structural members, such as in beams and columns, has shown that great ductility can be achieved with cracks that are barely visible to the naked eye [2]. While these characteristics have enormous potential, their promise has not yet been fully realized.

In recent years, more and more design codes and recommendations have included provisions for the use of fibers as a reinforcing material [3–9]. For safe and efficient design with this new material, it is critical to properly account for fiber distribution and orientation within structural components. Previous research has demonstrated that the strength of FRC members is very dependent on fiber orientations [10–12]. These fiber orientations are often highly anisotropic in nature and are the result of material flow patterns during the casting process [12, 13].

The objective of the work described in this paper is to characterize and quantify the alignment of fibers in ultra-high performance concrete (UHPC). Specimens were prepared under different casting conditions to produce different distributions of fiber orientation. The significance of this work is that a thorough understanding of the role of fiber orientation is necessary both for accommodation of these materials in building codes, but also for quality control purposes when a small sample of the material (cast or cored) is used to verify characteristics of the larger structure.

1.2 X-ray computed tomography (CT) in concrete research

X-ray computed tomography has been applied to concrete research problems for over 30 years [14, 15]. The ability to locate and identify internal material features is in itself a powerful feature; however, the 3D digital images that result from modern CT instruments allow for the exploitation of image analysis techniques that can lead to high resolution measurements [16]. These techniques have been applied to a number of concrete materials problems, including concrete pore structure [17, 18], sulfate attack [19], and fracture [20, 21].

These techniques are particularly well suited for FRC. Fibers can be identified, measured, and characterized according to spatial distribution as well as directional orientation [22–24]. These techniques are also well suited for characterizing features of irregular geometry.

2 Materials

Cor-Tuf was selected as the FRC mix for this investigation. Cor-Tuf is the name that was given to a family of ultra-high performance concretes (UHPCs) developed at the U.S. Army Engineer Research and Development Center (ERDC). Cor-Tuf is distinguished by a high compressive strength, which generally ranges from around 190 to 244 MPa [25, 26]. Cor-Tuf can be broadly characterized as a reactive powder concrete (RPC) with a maximum particle size of approximately 0.6 mm [26]. This maximum particle size is governed by the maximum size of the foundry grade Ottawa sand used in the mix.

The water-to-cement ratio used in Cor-Tuf is limited to about 0.21, and the ratio of water to combined silica fume and cement is 0.158. The water-to-cement ratio of Cor-Tuf is far lower than that representative of conventional concretes, which generally have a water-to-cement ratio near 0.40 [26]. The volumetric content of fibers in Cor-Tuf is 3.15%. This is somewhat higher than the volumetric fiber content recommended for most typical FRC applications [26]. This UHPC has been the subject of extensive research and use by the US Army Corps of Engineers over a number of years and, thus, despite the uncommonly high fiber content, study of its properties and performance continues to be of significant interest.

The steel fibers used in the making of Cor-Tuf are the Dramix® 3D-55/30 BG (also known as ZP-305) product of N.V. Bekaert S.A. (Fig. 1). These fibers were selected by the ERDC for inclusion within the Cor-Tuf mixture primarily because of their low cost
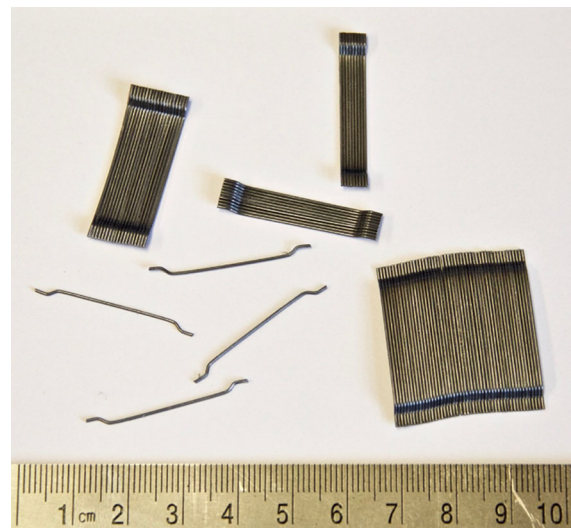

Fig. 1 Bekaert Dramix® 3D-55/30 BG steel fibers (diameter: 0.55 mm; length: 30 mm; tensile strength: 1100 MPa)

and easy attainability. The hooks at the ends of these fibers are intended to provide additional anchorage between the fiber and the concrete matrix during fracture and, through this anchorage, to facilitate higher levels of tensile deformation in the straight, central section of the fibers prior to failure [27]. These fibers come from the manufacturer adhered together in bundles using a water soluble adhesive. During the concrete mixing process, the adhesive is dissolved and the fibers are dispersed. These fibers are approximately 30-mm long, and each fiber has a diameter of approximately 0.55 mm [28]. The fibers are hooked at each end, and the tensile strength of each fiber is approximately 1100 MPa [28].

3 Methods

3.1 Samples

A series of factors related to the X-ray CT system and the mechanical loader available for use during these experiments imposed limitations on the possible sample size. First, given the high compressive strength of the Cor-Tuf material, it was calculated that the failure load of compression samples larger than 70 mm in diameter could exceed the maximum capacity of the available loading system. This was of critical importance since some of these samples would later be subjected to incremental compressive loading up to failure with CT scans collected after each loading step to measure crack growth. It was also found that the quality of the CT images began to significantly deteriorate for Cor-Tuf samples with diameters exceeding approximately 76 mm. This was thought to be related to a number of contributing factors including insufficient X-ray penetration, cone-beam artifacts, and decreased image resolution.

Given these limitations, a nominal sample diameter of 70 mm was selected for the first set of experiments. A specific representative volume element (RVE) for the Cor-Tuf material does not appear to have ever been precisely defined. The determination of an optimal RVE is further complicated by the fact that multiple definitions for determining the RVE currently exist [29–31]. Further, any RVE based purely on the size of material components, such as fibers, would not sufficiently capture the effects that more global phenomena, such as material flow, have on fiber

distribution and orientation characteristics during the casting process. Given the complexity in determining an optimal RVE and the limitations of the testing equipment, cylinders with 70 mm diameters were considered to provide a reasonable sample of the material given that the minimum dimension of these samples exceeded the length of the largest material component, the fibers, by more than a factor of two.

These cylindrical samples of Cor-Tuf were cut from cores drilled out of the middle of a thick concrete slab rather than cast in cylindrical molds. This was done, so that the structure of the material within the cylinders would most closely represent concrete properties in actual structural members. This ensured that the orientation of fibers would not be constrained by the boundaries of small casting molds. The Cor-Tuf slab was 914-mm wide by 914-mm long by 556-mm deep and cast directly from a concrete mixing truck. All cylinders were collected from locations at least 76 mm from the external edges of the slab to ensure that edge effects on fiber orientation were minimized.

After the coring process was completed, samples were cut to different lengths, and their ends were ground. Sample sizes were selected as necessary for the completion of unconfined compression tests (nominally 70-mm diameter by 140-mm height) and double punch tests (nominally 70-mm diameter by 70-mm height). Table 1 provides a detailed overview of the properties of all samples analyzed in this paper. Figure 2 provides example images of a cast and a cored sample, respectively.

A second set of cylindrical samples was also cast from Cor-Tuf. These samples, however, were cast individually using small plastic molds. Each sample also contained a 9.5-mm diameter reinforcing bar centered within its cylindrical cross section and embedded 121 mm. This configuration enabled X-ray CT observation of damage resulting from reinforcing bar pull-out. The results of these pull-out experiments will also not be discussed in this paper, but have already been published elsewhere [32, 33].

This second set of samples represented a contrast to the first set in that their fiber orientations were highly confined by the plastic molds and the reinforcing bars. Additionally, these samples were cast by hand using small scoops rather than poured directly from a concrete mixing truck. The Cor-Tuf samples containing reinforcing bars were cast into cylindrical molds that were slightly larger in diameter (nominally

Table 1 Sample properties

Sample name	Fabrication method	Embedded reinforcing bar	Diameter (mm)	Height (mm)	CT image resolution (μm)
C10M	Cored	No	70.4	140.5	46
C13M	Cored	No	70.3	141.3	46
C15M	Cored	No	70.5	142.1	48
C11M	Cored	No	70.5	70.6	32
C12M	Cored	No	70.4	70.5	33
C16M	Cored	No	70.4	70.4	33
CRF1	Cast	Yes	76.2	152.4	53
CRF2	Cast	Yes	76.2	152.4	53
CRF3	Cast	Yes	76.2	152.4	53
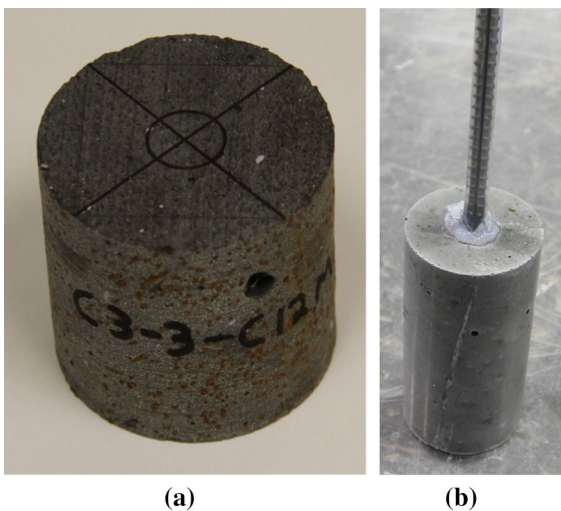
Fig. 2 Example images from a cored (**a**) and a cast (**b**) sample

76 mm) than the cored samples. The height of these samples was nominally 152 mm. This allowed for the use of standard molds and facilitated easier placement of the Cor-Tuf around the reinforcing bars during casting.

Unfortunately, the mechanical characterization procedures carried out on the cast and cored specimens are not directly comparable. This is because the cast and cored samples were originally fabricated for separate testing programs, which is also the reason for their slightly different sizes. While the cored specimens were subjected to compression and tensile testing, the cast specimens were only subjected to reinforcing-bar pull-out testing. For this reason, no results from the mechanical testing programs are presented in this paper. These results have, however,

been published in previous papers concerning the separate research programs [32–34].

3.2 CT scanning and image analysis

During X-ray CT scanning, a sample is placed on a rotating table between an X-ray source and an X-ray detector (Fig. 3) [35]. This causes an X-ray attenuation image of the sample to be projected upon the detector. By recording these projected images during the 360° rotation of the sample, mathematically-based reconstruction algorithms can be used to produce a three-dimensional representation of X-ray attenuation within the sample [36]. The X-ray attenuation, which is roughly correlated with density, of individual component materials within the sample can then be identified and objects made from these component materials can be individually separated and analysed.

The scanning system that was used during all X-ray CT experiments was located at the University of Florida. A 225-kV microfocus X-ray tube manufactured by Comet GmbH was used to generate the X-ray beam. The flat panel detector was manufactured by Thales Electron Devices and had an active image sensor area of 285 mm × 406 mm with an array of 2240 × 3200 pixels and a pixel size of 127 μm [37]. The 3D-CT images were reconstructed using the program efX CT [38]. All subsequent image analysis was completed in MATLAB [39]. An example cross section from a typical CT image of a Cor-Tuf sample is provided in Fig. 4.

Given the large size of the data sets and the computational resources available, during fiber analysis a decision was made to reduce the resolution of
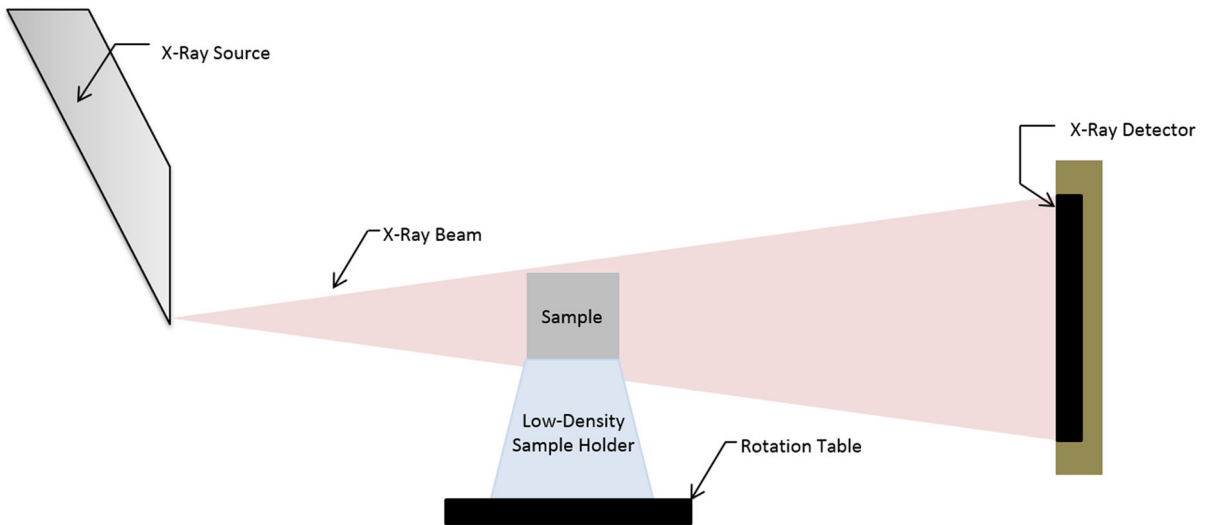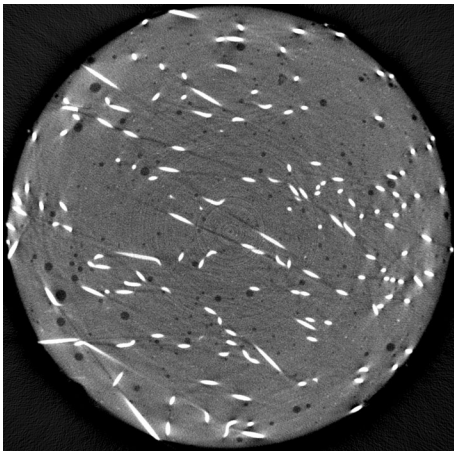
Fig. 3 X-ray CT configuration

Fig. 4 Example slice taken from a CT image of the internal structure of sample C11 M

the CT images by a factor of two through a process of pixel averaging (also called binning). This resolution was considered sufficient for fiber orientation analysis since, even for the images with the most coarse resolution, the fibers were easily identifiable, possessing a diameter of more than 5 image voxels (a voxel is a 3D pixel). This binning process also produced smoother images with a higher signal-to-noise ratio.

The first step of the fiber analysis was to identify and separate fiber voxels from all other image voxels. For this purpose, a threshold had to be selected and subsequently used for image binarization, with all voxels darker than the threshold transformed to black

and all voxels lighter than the threshold transformed to white. Given that this threshold had to be consistently applied for a large range of datasets, an automated selection method was implemented.

The first step in this process was to calculate a histogram of voxel brightness for all image voxels. Using the Triangle selection algorithm [40, 41], a virtual line was drawn from the right axis of the image histogram (which represented a consistent X-ray attenuation for all samples) to the top of the largest histogram peak (excluding the initial peak at zero, which represents air voxels) (Fig. 5). A calculation was then conducted to determine which point on the histogram was furthest from the virtual line in the
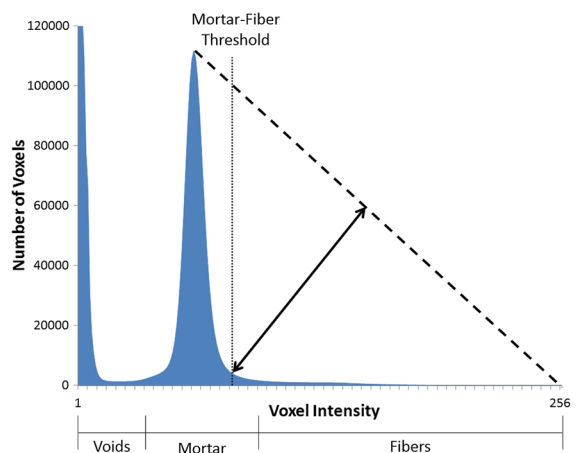

Fig. 5 Mortar-fiber threshold definition

direction perpendicular to it. The location of that point was identified as the mortar-fiber threshold.

During the fiber analysis, it became clear that a significant reconstruction artifacts had to be corrected before accurate fiber characteristics could be measured. These artifacts resulted in much thicker fibers along the edge of the sample compared to those in the center because of edge brightening in the 8-bit images (Fig. 6). This effect was successfully removed, however, by creating an algorithm that measured fiber diameters in each 2D slice throughout the image (by means of a connected-components analysis) and interatively adjusted 2D polynomial image filters on a slice-by-slice basis until all fiber diameters converged to the actual fiber diameter, which could be calculated in voxels based on the diameter of a 3D-55/30 BG fiber (550 μm) divided by the resolution of the individual scan.

Prior to the orientation analysis, the greyscale CT images were smoothed using a Gaussian kernel with a width approximately equal to the fiber diameter in voxels. Such smoothing operations have been shown to improve the results of the second order image differentiation that is necessary for Hessian-based orientation analysis (described below) [42, 43].

The orientation analysis was completed using the Hessian-based method [42, 43]. In this method, the X-ray CT images are considered to be 3D functions that are twice differentiable in all directions [44]. By calculating the Hessian matrix (Eq. 1), partial second derivatives of intensity can be computed for all fiber voxel points.

$$H = \begin{bmatrix} \dfrac{\partial^2 I}{\partial x^2} & \dfrac{\partial^2 I}{\partial x \partial y} & \dfrac{\partial^2 I}{\partial x \partial z} \\ \dfrac{\partial^2 I}{\partial y \partial x} & \dfrac{\partial^2 I}{\partial y^2} & \dfrac{\partial^2 I}{\partial y \partial z} \\ \dfrac{\partial^2 I}{\partial z \partial x} & \dfrac{\partial^2 I}{\partial z \partial y} & \dfrac{\partial^2 I}{\partial z^2} \end{bmatrix} \tag{1}$$

H Hessian matrix, I grayscale sample image matrix.

At a point within a fiber, the second derivative of intensity in the direction of the longitudinal axis of the fiber will be much less than those in the transverse directions. The orientation of fibers can, thus, be calculated by computing the eigenvalues and eigenvectors of the Hessian matrix (Fig. 7). The primary fiber orientation recorded at a single point is, therefore, the eigenvector corresponding to the smallest eigenvalue [44].

During the orientation analysis, the corrected binary images of the fibers were used to identify the fiber voxels, but the actual Hessian-matrix calculations were carried out on the original, unadjusted greyscale CT images. This was because the image-artifact removal was carried out on a slice by slice basis over the sample height. Thus, there was a possibility that individual horizontal slices might vary in brightness. This could cause an artificial gradient in intensity in the vertical direction and, thus, slightly horizontally skew fiber orientations in the results, since the eigenvector corresponding to the smallest eigenvalue of the Hessian matrix would tend to be oriented perpendicular to this gradient.

Eigenvectors and eigenvalues of the Hessian matrix were computed for all voxels corresponding to fiber material within the X-ray CT images using the

Fig. 6 Comparison of a single slice of the fibers image before (left) and after (right) correction based on fiber diameter
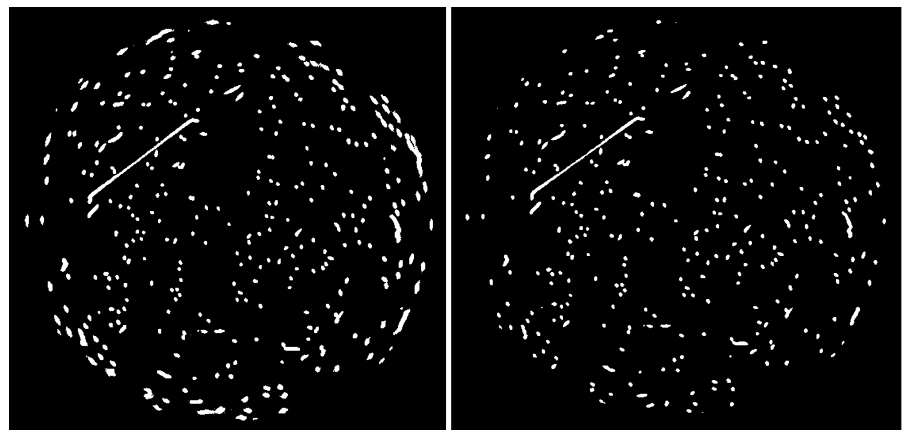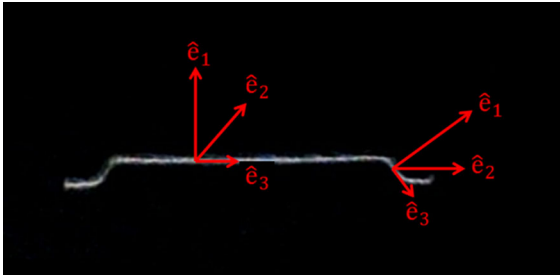
Fig. 7 Eigenvectors of the Hessian matrix at two points within a fiber

modified version of a MATLAB algorithm originally developed at the University of Maine [43, 45]. Various methods exist to depict and analyze orientation data in three dimensions. For the present analysis, coordinates have been converted from a Cartesian to a spherical system [46]. In this spherical coordinate system, orientations are characterized by angles θ and Φ (Fig. 8). The angle θ represents the azimuthal angle in the x–y plane from the x-axis (in this context the cylindrical axis of the sample is denoted as the z-axis), with $0 < \theta < 360°$ (Eq. 3). The angle Φ represents the polar angle from the positive z-axis. Since the fibers are symmetric about their lengths, a symmetry condition is likewise imposed on Φ, with $0 < \Phi < 90°$ (Eq. 4).

$$r = \sqrt{x^2 + y^2 + z^2} \qquad (2)$$

$$\theta = tan^{-1}\left(\frac{y}{x}\right) \qquad (3)$$
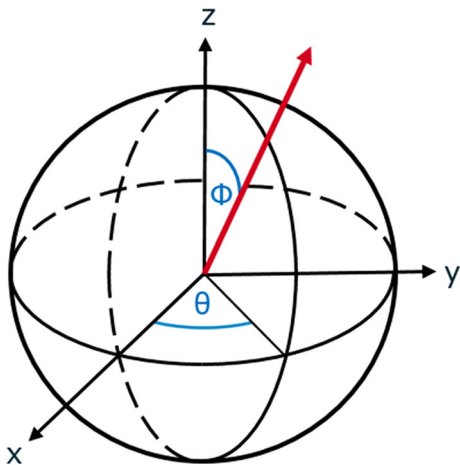

Fig. 8 Spherical coordinate system

$$\Phi = cos^{-1}\left(\frac{z}{r}\right) \qquad (4)$$

Since the fiber orientation analysis was conducted on a voxel-by-voxel basis, the resulting measurements contained not only orientation values related to the long axis of the fibers, but also orientation measurements related to the hooks, as demonstrated in Fig. 7. Given that the size of the hooks relative to the overall fiber dimensions was relatively small (Figs. 1 and 7), the resulting orientation values were considered to be broadly representative of overall fiber field orientation. Although these hook effects could theoretically be eliminated through the identification and skeletalization of individual fibers and an evaluation of the global orientation of each, such a process was never successfully implemented for this analysis because of the complexity of the internal material structure. Given the relatively high density of fibers within the material, large numbers of fibers were found to be in contact with one another and very difficult to digitally separate during analysis. It was also found that within the samples some fibers remained adhered to one-another even after the adhesive binding the rest of the fibers into bundles had dissolved during the mixing process.

More detailed information about equipment settings, segmentation techniques, artifact corrections, and orientation analysis can be found in [32].

4 Results

Figures 9 and 10 provide visualizations and orthogonal projections of the fiber orientation data for both a typical cored and a typical cast sample. From Fig. 9 it is clear that for the cored sample C12 M, a highly anisotropic fiber field existed with primary orientation direction of roughly $\theta = 345°$ and $\Phi = 45°$. For the cast sample CRF2, however, the fiber orientation field appeared much more heterogeneous with only minor concentrations in the orthogonal projections (Fig. 10).

Although the results of Figs. 9 and 10 clearly display the fiber orientation characteristics of individual samples, a further method must be developed for comparing the characteristics of large numbers of FRC samples. One method commonly used for such comparisons is the calculation and comparison of the order parameter (S) and the biaxiality parameter (b_s)
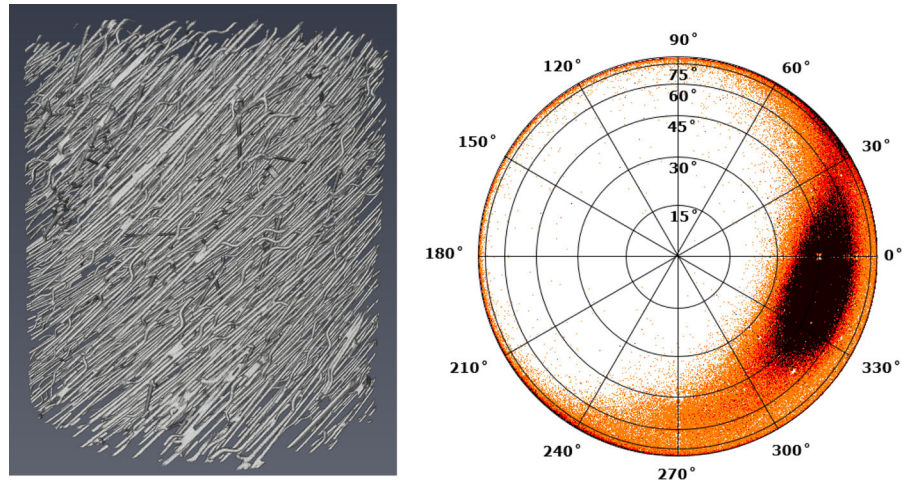
Fig. 9 Example side view of fiber rendering for sample C12M (left) and orthographic projection of fiber orientation distribution (right). Projection radius: $0 < \Phi < 90°$; projection circumference: $0 < \theta < 360°$

Fig. 10 Example side view of fiber rendering for sample CRF2 (left) and orthographic projection of fiber orientation distribution (right). Projection radius: $0 < \Phi < 90°$; projection circumference: $0 < \theta < 360°$
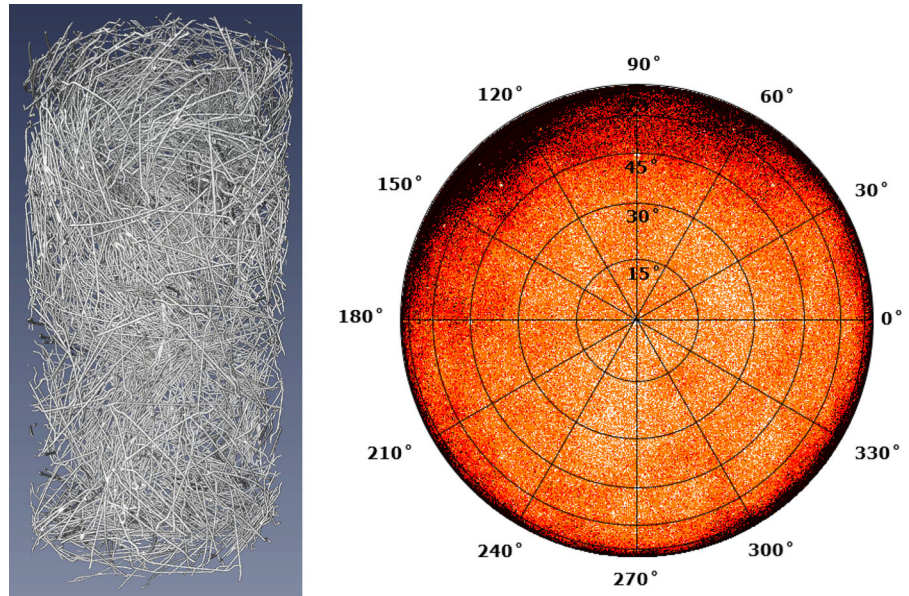

[42, 47, 48]. In this method, the fiber orientation distributions are characterized by an alignment tensor **A** (Eq. 5), which is calculated directly from the second-order orientation tensor **O** (Eq. 6).

$$A = O - \frac{1}{3}I \qquad (5)$$

where

$$O = \frac{1}{N}\sum_{i}^{N} n^i \otimes n^i \qquad (6)$$

n^i the orientation vector of the ith fiber voxel, I second-order identity tensor, N the total number of fiber voxels.

The order parameter, S, (Eq. 7) and signed biaxiality parameter, b_s, (Eq. 8) can then be calculated using the sorted eigenvalues of the alignment tensor $(|\lambda_1| \geq |\lambda_2| \geq |\lambda_3|)$. The order parameter, S, has a range of $[-0.5, 1]$, where a value 1 corresponds to well-aligned fibers, 0 corresponds to isotropically oriented fibers, and -0.5 corresponds to alignment of all fibers along a single plane [42]. The signed biaxiality parameter, b_s, has a range of $[-\frac{1}{3}, \frac{1}{3}]$, where the closer that the value is to 0, the greater the rotational

symmetry of the orientation distribution about the eigenvector corresponding to λ_1.

$$S = \frac{2}{3}\lambda_1 \tag{7}$$

$$b_s = \frac{1}{2}(\lambda_3 - \lambda_2) \tag{8}$$

As described in Sect. 3.1, this fiber analysis included cored samples of two different heights as well as cast samples. In both Figs. 11 and 12, the order and biaxiality parameters for longer cored samples (fabricated for unconfined compression testing—reference dimensions in Table 1) are recorded on the left (C10M, C13M, and C15M), shorter cored samples (fabricated for double punch testing) are recorded in the center (C11M, C12M, and C16M), and individually cast samples are recorded on the right (CRF1, CRF2, and CRF3).

It is clear from Fig. 11 that the cored samples exhibited consistently higher order parameter values than the individually cast samples, which is corresponds to higher levels of anisotropy. The cored samples also exhibited consistently lower levels of rotational symmetry than the individually cast samples, as demonstrated by the signed biaxiality factor (Fig. 12).

It is thought that the highly anisotropic fiber orientations seen in the cored samples are due to the casting process itself. Since the fibers are long and

slender, it is thought that they align themselves with the direction of concrete flow and, thus, are poured into the forms already with an anisotropic orientation. This explanation is supported by the findings of other research conducted using FRC [12, 13]. This issue is of critical importance to the use of FRC since, although fibers oriented perpendicular to crack openings improve tensile and ductile performance, those oriented parallel may actually reduce tensile strength and ductility.

This is because, when fibers are oriented perpendicular to the axis of primary tensile stress (such as in the bottom of a beam), any cracks that arise will have similar orientation characteristics to the fibers and, thus, will not be inhibited in their growth since they will almost never cross the surrounding fibers. Thus, the tensile strength of such a component could remain relatively unaffected even by a high content of fibers. It is even possible that the tensile strength of such a component would actually decrease as a result of the fibers because a relatively weak bond between the fibers and the mortar could actually serve as a plane of weakness that fosters the earlier formation and growth of tensile cracking.

One promising approach for ensuring consistent and predictable fiber orientation would be to implement casting methods that optimize the anisotropic orientation of the fibers relative to the plane of primary loading. By casting long flexural members, such as beams, from the end rather than the center, for
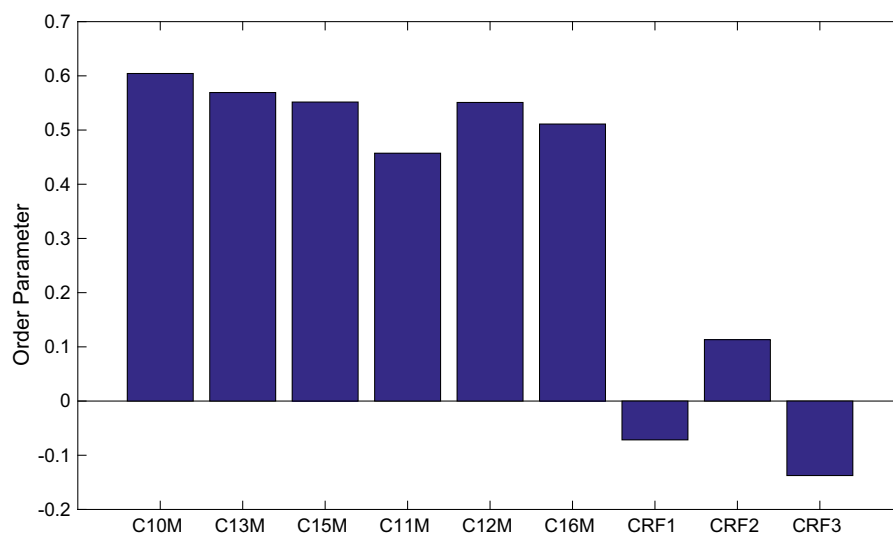

Fig. 11 Order parameter calculated for both cored (C10M–C16M) and cast (CRF1–CRF3) Cor-Tuf samples
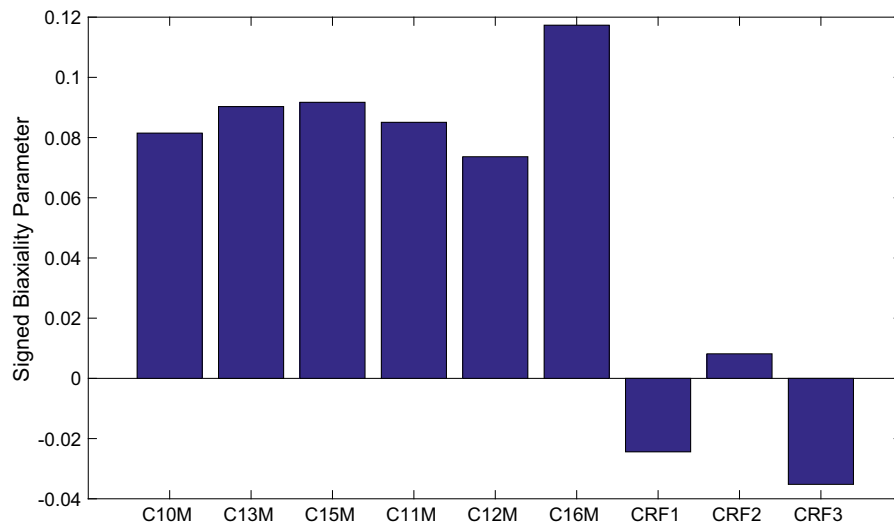
Fig. 12 Signed biaxiality parameter calculated for both cored (C10M–C16M) and cast (CRF1–CRF3) Cor-Tuf samples

instance, so that longitudinally-oriented fibers along the surface of the members would result, which would be optimal for carrying tensile load across surface cracks [49]. Such a method could be particularly effective for casting components with consistent shape, such as standard AASHTO beam shapes, since an optimized casting procedure could be developed, verified through testing, and then repeated. The results of further casting optimization studies could be used to create provisions for FRC that specify the optimal location of concrete entry into the formwork based on the dimensions, aspect ratio, fiber size, and amount of reinforcing.

Although a theoretical, alternate approach would be to ensure heterogeneous fiber orientations (for instance through pre- or post-casting agitation of the concrete), such a method would be very difficult to implement in practice. This is especially true since any material flow subsequent to agitation would have to be prevented since it could lead to re-alignment of the fibers in the material.

The dependence of material performance upon highly anisotropic fiber distributions indicates that individually cast cylinders for material characterization and quality assurance are unlikely to provide an accurate representation of the actual material in FRC structural components. Thus, alternative sampling and testing methods may be necessary for evaluating FRC strength and performance characteristics if FRC is to become a widely used construction material. Tensile

material tests that are able to account for anisotropic fiber orientation, such as the Multidirectional Double Punch Test (MDPT) and the Double Edge Wedge Splitting (DEWS) test, should be assessed in further detail as possible alternatives to current tensile property testing methods [12, 13]. Cored samples may be necessary for accurate characterization, collected either from within the actual member being characterized or from within a test specimen cast with similar flow-pattern characteristics.

The present study was not focused on correlating mechanical performance properties with fiber orientations. Such research needs to be conducted, however, to quantify the level of dependence exhibited by material performance relative to varying fiber orientations and casting techniques. Using such data, more accurate numerical models of UHPC performance could be developed and used for the optimization of building code provisions.

Also of use to these numerical models would be statistical measurements of the correlation between crack orientation and fiber orientation. Such a study would require the precise identification and measurement of cracks. Accurate and consistent crack identification is difficult, however, because cracks are generally intertwined with the pores in the cement matrix. Recent research using digital volume correlation (DVC), however, has indicated the potential for highly accurate measurements of crack growth caused by loading when pre-loading and post-loading CT

images are compared [50]. The precise implementation of this method for concrete materials as well as the development of an accurate algorithm for measuring quantitative crack orientation properties should enable statistical analysis of this phenomenon.

5 Discussion

These experiments demonstrated the value of X-ray CT for evaluating the internal structure of FRC samples. Through the use of X-ray CT, it was possible to visually observe and quantify fiber orientation characteristics. Fiber orientation measurements extracted from the X-ray CT images of both cored and individually cast samples showed that the fiber distributions in cored samples exhibited consistently higher levels of anisotropy. As these cored samples were extracted from a slab cast directly from a concrete mixing truck, these results have implications for the use of FRC at the structural level.

These results indicate that the orientation of fibers within a specific portion of a structure is likely to be highly dependent on the casting method, the flow pattern of the material (including the effects of complex structural geometry and internal obstacles, such as reinforcing bars), and the compacting process. A detailed understanding of these phenomena is critical for both numerical modeling and for structural design since fibers oriented parallel to cracks tend to create zones of weakness, rather than strengthening the material. The results also provide evidence that traditional material characterization and quality control carried out using cast cylinders may be insufficient for evaluating the strength and performance characteristics of FRC in structural components.

Among the most important research topics for FRC is obtaining a better understanding of the effect of casting procedures on fiber distribution and orientation. Although much of this research can be completed through fluid mechanics modeling, experiments will also be required to validate the computational models. These experiments will need to investigate the effects of various casting methods on concretes with different fiber types and viscosities. These experiments will also need to account for the behavior of FRC cast in members of different sizes and shapes as well as with varying amounts of steel reinforcing bar.

Also of significant benefit, would be the investigation using X-ray CT of innovative, multi-axial material characterization tests that are better able to account for the effects anisotropy of fiber orientation than the uni-axial testing methods commonly in use at the present time. During these experiments, it would be ideal for concretes with varying strength and fiber reinforcement characteristics to be evaluated. By identifying more representative material characterization tests for FRC, safer and more efficient use of the material can be made in design and construction.

Compliance with ethical standards

Conflict of interest　The authors declare that they have no conflict of interest.

References

1. Borosnyoi A, Balazs GL (2005) Models for flexural cracking in concrete: the state of the art. J Struct Concr 6(2):1464–4177
2. Li VC, Mishra DK, Wu HC (1995) Matrix design for pseudo-strain-hardening fibre reinforced cementitious composites. Mater Struct 28(184):586–595. https://doi.org/10.1007/Bf02473191
3. ACI (2014) Building code requirements of for structural concrete. In: ACI 318-14. American Concrete Institute (ACI), Farmington Hill
4. CNR (2006) Istruzioni per la Progettazione, l'Esecuzione ed il Controllo di Strutture Fibrorinforzato. In: Riserche, C.N.d. (ed) CNR-DT 204, Italy
5. CPH (2008) Instrucción del Hormigón Estructural. In: Fomento, C.P.d.H.M.d. (ed) EHE-08, Spain
6. DBV (2001) DBV-Merkblatt Stahlfaserbeton. In: e.V., D.B.u.B.-V. (ed)
7. FIB (2013) fib model code for concrete structures 2010. In: Béton, F.I.d. (ed) Wilhelm Ernst & Sohn, Berlin, Germany, p 434

8. RILEM (2003) Test and design methods for steel fibre reinforced concrete; σ–ε design method: final recommendation; TC 162-TDF. Mater Struct 36:560–567

9. SIS (2014) Fibre concrete: design of fibre concrete structures. In: Institute, S.S. (ed) SS 812310

10. Barnett SJ, Lataste JF, Parry T, Millard SG, Soutsos MN (2010) Assessment of fibre orientation in ultra high performance fibre reinforced concrete and its effect on flexural strength. Mater Struct 43(7):1009–1023. https://doi.org/10.1617/s11527-009-9562-3

11. Ferrara L, Meda A (2006) Relationships between fibre distribution, workability and the mechanical properties of SFRC applied to precast roof elements. Mater Struct 39(4):411–420. https://doi.org/10.1617/s11527-005-9017-4

12. Pujadas P, Blanco A, Cavalaro SHP, de la Fuente A, Aguado A (2014) Multidirectional double punch test to assess the post-cracking behaviour and fibre orientation of FRC. Constr Build Mater 58:214–224. https://doi.org/10.1016/j.conbuildmat.2014.02.023

13. di Prisco M, Ferrara L, Lamperti MGL (2013) Double edge wedge splitting (DEWS): an indirect tension test to identify post-cracking behaviour of fibre reinforced cementitious composites. Mater Struct 46:1893–1918

14. Martz HE, Schneberk DJ, Roberson GP, Monteiro PJM (1993) Computerized-tomography analysis of reinforced-concrete. ACI Mater J 90(3):259–264

15. Morgan IL, Ellinger H, Klinksiek R, Thompson JN (1980) Examination of concrete by computerized-tomography. J Am Concr I 77(1):23–27

16. Landis EN, Keane DT (2010) X-ray microtomography. Mater Charact 61(12):1305–1316. https://doi.org/10.1016/j.matchar.2010.09.012

17. Bentz DP, Quenard DA, Kunzel HM, Baruchel J, Peyrin F, Martys NS, Garboczi EJ (2000) Microstructure and transport properties of porous building materials. II: three-dimensional X-ray tomographic studies. Mater Struct 33(227):147–153. https://doi.org/10.1007/Bf02479408

18. Landis EN, Petrell AL, Lu S, Nagy EN (2000) Examination of pore structure using three dimensional image analysis of microtomographic data. Concr Sci Eng 2(8):162–169

19. Stock SR, Naik NK, Wilkinson AP, Kurtis KE (2002) X-ray microtomography (microCT) of the progression of sulfate attack of cement paste. Cem Concr Res 32(10):1673–1675

20. Landis EN, Nagy EN, Keane DT, Nagy G (1999) A technique to measure three-dimensional work-of-fracture of concrete in compression. J Eng Mech 125(6):599–605

21. Poinard C, Piotrowska E, Malecot Y, Daudeville L, Landis EN (2012) Compression triaxial behavior of concrete: the role of the mesostructure by analysis of X-ray tomographic images. Eur J Environ Civ Eng 16:S115–S136. https://doi.org/10.1080/19648189.2012.682458

22. Bakshi SR, Batista RG, Agarwal A (2009) Quantification of carbon nanotube distribution and property correlation in nanocomposites. Compos Part A Appl Sci Manuf 40(8):1311–1318. https://doi.org/10.1016/j.compositesa.2009.06.004

23. Mishurova T, Rachmatulin N, Fontana P, Oesch T, Bruno G, Radi E, Sevostianov I (2018) Evaluation of the probability density of inhomogeneous fiber orientations by computed tomography and its application to the calculation of the effective properties of a fiber-reinforced composite. Int J Eng Sci 122(Supplement C):14–29. https://doi.org/10.1016/j.ijengsci.2017.10.002

24. Trainor KJ, Foust BW, Landis EN (2013) Measurement of energy dissipation mechanisms in the fracture of fiber-reinforced ultrahigh-strength cement-based composites. J Eng Mech 139(7):771–779

25. Roth JM, Rushing TS, Flores OG, Sham DK, Stevens JW (2010) Laboratory investigation of the characterization of Cor-Tuf flexural and splitting tensile properties. In: Army, U. (ed). Technical Report, Engineer Research and Development Center, Vicksburg, MS, USA

26. Williams EM, Graham SS, Reed PA, Rushing TS (2009) Laboratory characterization of Cor-Tuf concrete with and without steel fibers. In: Army U.S. (ed) Technical Report, Engineer Research and Development Center, Vicksburg, Mississippi, USA

27. Scott D, Long W, Moser R, Green B, O'Daniel J, Williams B (2015) Impact of steel fiber size and shape on the mechanical properties of ultra-high performance concrete. In: Army, U. (ed) Technical Report, Engineer Research and Development Center, Vicksburg, MS, USA

28. Bekaert (2012) Dramix® 3D-55/30 BG. In: N.V. Bekaert S.A

29. Drugan WJ, Willis JR (1996) A micromechanics-based nonlocal constitutive equation and estimates of representative volume element size for elastic composites. J Mech Phys Solids 44(4):497–524. https://doi.org/10.1016/0022-5096(96)00007-5

30. Hashin Z (1983) Analysis of composite-materials: a survey. J Appl Mech Trans ASME 50(3):481–505

31. Hill R (1963) Elastic properties of reinforced solids: some theoretical principles. J Mech Phys Solids 11(5):357–372. https://doi.org/10.1016/0022-5096(63)90036-X

32. Oesch TS (2015) Investigation of fiber and cracking behavior for conventional and ultra-high performance concretes using X-ray computed tomography. University of Illinois, Champaign

33. Oesch TS (2016) In-situ CT investigation of pull-out failure for reinforcing bars embedded in conventional and high-performance concretes. In: 6th conference on industrial computed tomography (ICT), Wels, Austria, February 9–12, 2016, vol 2. www.NDT.net

34. Oesch TS, Landis EN, Kuchma DA (2016) Conventional concrete and UHPC performance-damage relationships identified using computed tomography. J Eng Mech 142(12):04016101. https://doi.org/10.1061/(asce)em.1943-7889.0001168

35. Flannery BP, Deckman HW, Roberge WG, D'Amico KL (1987) Three-dimensional X-ray microtomography. Science 237(4821):1439–1444. https://doi.org/10.1126/science.237.4821.1439

36. Feldkamp LA, Davis LC, Kress JW (1984) Practical cone-beam algorithm. J Opt Soc Am A 1(6):612–619. https://doi.org/10.1364/JOSAA.1.000612

37. Thales (2003) FlashScan 35 Flat Panel Imaging System. In: User Manual, vol. 5.0.3. Thales Electron Devices

38. NSI (2008) efX CT. North Star Imaging, Inc., Rogers

39. Mathworks, T. (2018) MATLAB. In: Natick, MA, USA

40. Young IT, Gerbrands JJ, van Vliet LJ (1998) Fundamentals of image processing, 2.2nd edn. Delft University of Technology, Delft

41. Zack GW, Rogers WE, Latt SA (1977) Automatic measurement of sister chromatid exchange frequency. J Histochem Cytochem 25(7):741–753. https://doi.org/10.1177/25.7.70454

42. Herrmann H, Pastorelli E, Kallonen A, Suuronen J-P (2016) Methods for fibre orientation analysis of X-ray tomography images of steel fibre reinforced concrete (SFRC). J Mater Sci 51(8):3772–3783. https://doi.org/10.1007/s10853-015-9695-4

43. Trainor KJ (2011) 3-D analysis of energy dissipation mechanisms in steel fiber reinforced reactive powder concrete. University of Maine, Orono

44. Krause M, Hausherr JM, Burgeth B, Herrmann C, Krenkel W (2010) Determination of the fibre orientation in composites using the structure tensor and local X-ray transform. J Mater Sci 45(4):888–896. https://doi.org/10.1007/s10853-009-4016-4

45. Flanders LS (2014) LSFfiberOrient. In: MATLAB Program

46. Weisstein EW (2018) Spherical coordinates. http://mathworld.wolfram.com/SphericalCoordinates.html. Accessed 20 May 2018

47. Eppenga R, Frenkel D (1984) Monte-Carlo study of the isotropic and nematic phases of infinitely thin hard platelets. Mol Phys 52(6):1303–1334. https://doi.org/10.1080/00268978400101951

48. Steuer H (2004) Thermodynamical properties of a model liquid crystal. Technischen Universität Berlin, Berlin

49. Stahli P, Custer R, van Mier JGM (2008) On flow properties, fibre distribution, fibre orientation and flexural behaviour of FRC. Mater Struct 41(1):189–196. https://doi.org/10.1617/s11527-007-9229-x

50. Cinar AF, Hollis D, Tomlinson RA, Marrow TJ, Mostafavi M (2016) Application of 3D phase congruency in crack identification within materials. Paper presented at the 11th international conference on advances in experimental mechanics, Exeter, UK, 5th–7th September